Structural basis for KIT receptor tyrosine kinase inhibition by antibodies targeting the D4 membrane-proximal region

Andrey V. Reshetnyak[a,1], Bryce Nelson[b,1], Xiarong Shi[a], Titus J. Boggon[a], Alevtina Pavlenco[b], Elizabeth M. Mandel-Bausch[c], Francisco Tome[a], Yoshihisa Suzuki[c], Sachdev S. Sidhu[b,2], Irit Lax[a,2], and Joseph Schlessinger[a,2]

[a]Department of Pharmacology, Yale University School of Medicine, New Haven, CT 06520; [b]Donnelly Centre for Cellular and Biomolecular Research, University of Toronto, Toronto, ON, Canada M5S 3E1; and [c]Kolltan Pharmaceuticals, Inc., New Haven, CT 06520

Contributed by Joseph Schlessinger, September 19, 2013 (sent for review August 15, 2013)

Somatic oncogenic mutations in the receptor tyrosine kinase KIT function as major drivers of gastrointestinal stromal tumors and a subset of acute myeloid leukemia, melanoma, and other cancers. Although treatment of these cancers with tyrosine kinase inhibitors shows dramatic responses and durable disease control, drug resistance followed by clinical progression of disease eventually occurs in virtually all patients. In this report, we describe inhibitory KIT antibodies that bind to the membrane-proximal Ig-like D4 of KIT with significant overlap with an epitope in D4 that mediates homotypic interactions essential for KIT activation. Crystal structures of the anti-KIT antibody in complex with KIT D4 and D5 allowed design of affinity-matured libraries that were used to isolate variants with increased affinity and efficacy. Isolated antibodies showed KIT inhibition together with suppression of cell proliferation driven by ligand-stimulated WT or constitutively activated oncogenic KIT mutant. These antibodies represent a unique therapeutic approach and a step toward the development of "naked" or toxin-conjugated KIT antibodies for the treatment of KIT-driven cancers.

phosphorylation | therapeutic antibodies | cancer therapy | cell signaling | protein kinase

The receptor tyrosine kinase (RTK) KIT is a transmembrane protein that plays crucial roles in mediating diverse cellular processes including cell differentiation, proliferation, and cell survival, among other activities. These processes occur through activation of KIT upon binding by stem cell factor (SCF), a ligand found in membrane-anchored and soluble forms (1, 2) in a variety of cell types, including hematopoietic stem cells, germ cells, vascular endothelial cells, and the mesenchymal cells with uniquely neuromuscular differentiation known as the interstitial cells of Cajal (3, 4). KIT belongs to the type III subfamily of RTKs (5), a family composed of an extracellular region that includes five Ig-like domains (designated D1–D5), a single transmembrane domain (TM), a juxtamembrane region (JM), a tyrosine kinase domain split by a kinase insert, and a C-terminal tail (6) (Fig. 1*A*).

Based on the determination of the crystal structure of the complete extracellular region of KIT before and after ligand stimulation (7), and the tyrosine kinase domain (8, 9), a mechanism has been proposed whereby activation of KIT is initiated through receptor dimerization (10). Dimerization of the KIT ectodomain is ligand-driven and initiated through high-affinity binding of an SCF dimer to the membrane distal Ig-like domains (D1–D3) of the receptor (11, 12). Cross-linking of the membrane distal Ig-like domains with their ligand dramatically increases local concentration of the membrane-proximal (D4 and D5) and TMs to enable homotypic contacts by weak D4–D4 and D5–D5 interactions between neighboring KIT molecules. These homotypic associations promote conformational rearrangements that permit correct association between neighboring cytoplasmic regions of KIT dimers resulting in autophosphorylation, tyrosine kinase stimulation, recruitment of signaling proteins, and cell signaling.

Dysregulation of KIT, by a variety of different somatic as well as rare germ-line mutations, has been associated with numerous hematopoietic and other cancers, including gastrointestinal stromal tumors (GIST), a subset of melanomas, systemic mastocytosis, and acute myeloid leukemia. Most reoccurring activating mutations map to the cytoplasmic JM region (exon 11) and to the membrane-proximal Ig-like domain D5 (exon 9) of the extracellular region (13, 14). Currently, initial treatment for patients with GIST involves the small-molecule kinase inhibitor Gleevec (imatinib), which can efficiently block kinase activity of JM and D5 mutants of KIT. Unfortunately, most patients with GIST develop resistance to the drug within 2 y of treatment by acquiring additional mutations usually mapped to exons 13 and 14 (V654A and V670I, respectively). Patients resistant to Gleevec are usually treated with the kinase inhibitor Sutent (sunitinib), which can more efficiently inhibit WT KIT protein as well as many of the mutations that confer imatinib resistance. In addition to Gleevec-resistant mutations in exons 13 and 14, kinase domain mutants (exon 17) that are resistant to Gleevec and Sutent are also seen in patients with GIST (15).

Several mAbs targeting RTKs have shown promising results as anticancer therapies, including mAbs against members of the

Significance

The receptor tyrosine kinase KIT is aberrantly activated primarily by somatic mutations in gastrointestinal stromal tumors and in a subset of acute myeloid leukemia, melanoma, and other cancers. Treatment of these cancers with tyrosine kinase inhibitors shows durable clinical response, but drug resistance and disease progression eventually occur in all patients. Here we describe monoclonal antibodies that block the activity of KIT and its oncogenic mutant. Structural and biochemical analyses of anti-KIT antibodies in complex with a KIT fragment demonstrated that KIT antibodies bind to a critical Achilles heel region that is essential for receptor activation. These antibodies may provide a potentially unique therapeutic approach for the treatment of tumors driven by WT or oncogenically mutated KIT.

Author contributions: A.V.R., B.N., Y.S., S.S.S., I.L., and J.S. designed research; A.V.R., B.N., X.S., A.P., E.M.M.-B., F.T., and I.L. performed research; A.V.R., B.N., T.J.B., Y.S., I.L., and J.S. analyzed data; and A.V.R., B.N., S.S.S., I.L., and J.S. wrote the paper.

The authors declare no conflict of interest.

Data deposition: The atomic coordinates and structure factors have been deposited in the Protein Data Bank, www.pdb.org (PDB ID codes 4K94 and 4K9E).

[1]A.V.R. and B.N. contributed equally to this work.

[2]To whom correspondence may be addressed. E-mail: sachdev.sidhu@utoronto.ca, irit.lax@yale.edu, or joseph.schlessinger@yale.edu.

This article contains supporting information online at www.pnas.org/lookup/suppl/doi:10.1073/pnas.1317118110/-/DCSupplemental.

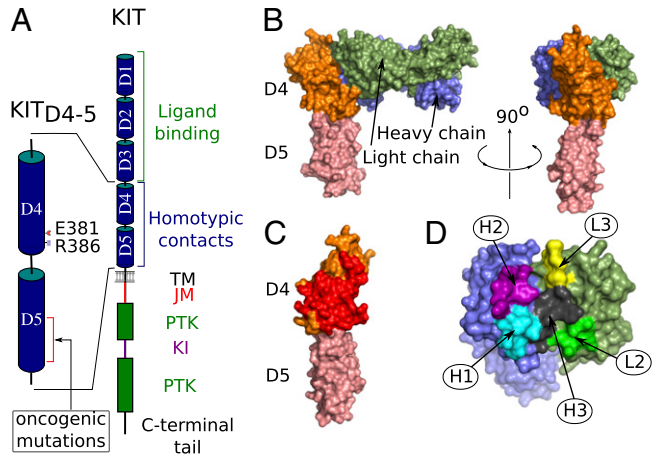

Fig. 1. Structure of the Fab19–KIT$_{D4-5}$ complex. (*A*) Schematic representation of WT KIT as well as the KIT$_{D4-5}$ fragment that was used in this study. Glu381 and Arg386, residues important for KIT activation, are marked on KIT$_{D4-5}$ fragment. D1 to D5 are Ig-like domains 1 to 5 respectively. JM, juxtamembrane; KI, kinase insert; PTK, protein tyrosine kinase domain; TM, transmembrane. (*B*) Surface representation of Fab19–KIT$_{D4-5}$ complex. (*Left*) View following 90° rotation along the shown axis. D4 and D5 of KIT are colored with orange and pink, and heavy and light chains of Fab19 with blue and green, respectively. The regions of interactions between Fab19 and KIT$_{D4-5}$ are visualized in "open-book" format for D4 (*C*) and Fab (*D*). The buried surface area on the D4 side is shown in red in *C* and is in the same scale as in *B*. The interactions between Fab19 and D4 are mediated by CDR loops and surrounding residues. The buried interface surface of the Fab19 is color coded by CDR: H1, cyan; H2, magenta; H3, gray; L2, bright green; L3, yellow (*D*). Fab19 in *D* is enlarged compared with images in *B* and *C*.

EGFR family of RTKs, which were approved for clinical use, including cetuximab and panitumumab (anti-EGFR mAbs), as well as trastuzumab and pertuzumab (anti-ErbB2 mAbs) (16, 17). Antibodies can be highly specific for their targets, and therefore off-target side effects are reduced compared with small-molecule kinase inhibitors. Specific targeting of oncogenic RTKs by inhibitory mAbs may allow the resistance that frequently occurs in patients treated with kinase inhibitors to be surmounted.

We have shown previously that homotypic interactions between the membrane-proximal domains of KIT (D4 and D5) are critical for receptor activation and that disruption of the D4–D4 interface strongly compromises receptor activation (7). As KIT oncogenic mutants located in D5 are dependent on homotypic contacts between neighboring ectodomains, it is reasonable to expect that activation of these mutants could be inhibited by monoclonal antibodies directed against KIT domains D4 or D5. Here, anti-KIT antibodies were isolated from a naive, phage-displayed synthetic antibody library. Crystal structures of a fragment antigen-binding (Fab) in complex with KIT membrane-proximal domains D4 and D5 (KIT$_{D4-5}$) revealed binding to D4 that overlapped significantly with an epitope required for homotypic interactions essential for SCF-dependent KIT activation. Furthermore, information obtained from the structure of antibody in complex with KIT was applied to guide the design of affinity maturation libraries, enabling isolation of antibody variants with increased binding affinity equating to increased efficacy. These antibodies were capable of efficient inhibition of KIT activity that led to suppression of cell proliferation and provide a potentially unique therapeutic approach for the treatment of tumors driven by WT or aberrantly activated KIT mutants.

Results

The two membrane-proximal Ig-like domains of KIT (KIT$_{D4-5}$ fragment; Fig. 1*A*) determined structurally to be critical for KIT activation (7) were used as an antigen to isolate binding Fabs from a naive phage-displayed library (library F; Fig. S1) containing more than 10^{10} unique clones (18, 19). The binding properties of the phage-derived Fabs were compared with the binding properties of a murine monoclonal anti-KIT antibody designated KTN37 that was obtained by immunization of mice with the same antigen. A variety of in vitro binding experiments using 3T3 cells ectopically expressing WT KIT demonstrated that the phage-derived Fabs and the KTN37 mAb bind specifically to D4 of recombinant isolated KIT or to native KIT molecules expressed on the cell surface of live cells. The structure of one of the most potent phage-derived Fab, designated Fab19 (Fig. S1), in complex with KIT$_{D4-5}$ (Fig. 1*A*), was further analyzed by X-ray crystallography.

The Structure of Fab19–KIT$_{D4-5}$ Complex. A purified complex composed of Fab19 together with KIT$_{D4-5}$ was subjected to extensive screening for crystal growth and further optimization. We obtained crystals that belong to the *C*2 space group with a single 1:1 complex of KIT$_{D4-5}$ and Fab19 in the asymmetric unit. The structure of this complex was determined to 2.4-Å resolution (*SI Materials and Methods*, Fig. 1*B* and Table S1).

The overall structure of KIT$_{D4-5}$ bound to Fab19, is very similar to the structures of these two Ig-like domains observed previously as part of the structures of full-length extracellular region of KIT alone, or in complex with SCF [Protein Data Bank (PDB) ID codes 2EC8 and 2E9W; ref. 7]. Superposition of individual D4 and D5 from Fab19–KIT$_{D4-5}$ complex structure with corresponding domains of KIT ectodomain structure (PDB ID code 2EC8) revealed rmsd values of 0.65 Å for 96 and 59 Cα residues in D4 and D5, respectively. The structure revealed Fab19 binding exclusively to D4 of KIT with a buried surface of 1,029 Å^2 on the D4 side of the interface (Fig. 1*C* and Table S2). Nearly the entire β-sheet of D4 (one of two β-sheets in Ig-like domain), including βA, βB, β, and βD, as well as the AA′, A′B, EF, and DE loops, was buried under the Fab19 surface (Fig. 1*D* and Fig. S2).

The majority of the contacts were made by the heavy chain of the Fab (800 Å^2 vs. 283 Å^2 for the light chain; Fig. 1*D*, Fig. S2, and Table S2), with most key interactions mediated by the complementarity-determining region (CDR) loops of the Fab, including all three CDRs of the heavy chain and L2 and L3 of the light chain. The majority of the specificity-determining contacts came from CDRs H2 and H3 (additional details about Fab19–D4 interface is described in *SI Appendix*).

Fab19 Contacts Critical for KIT Receptor Inhibition. We have shown previously that D4–D4 homotypic interactions mediated by two salt bridges between Arg381$^{D4'}$ and Glu386^{D4}, both located in the

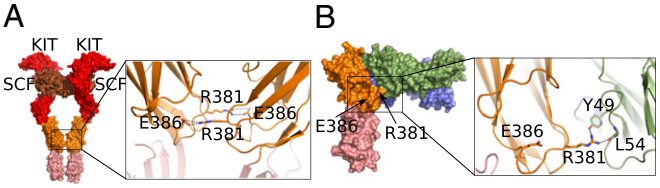

Fig. 2. D4–D4 homotypic interactions are occluded by Fab19 binding. (*A*, *Left*) Surface representation of KIT–SCF 2:2 complex. D4 and D5 are colored as in Fab19–KIT$_{D4-5}$ complex in Fig. 1; D1, D2, and D3 are in red, and SCF is in brown. (*A*, *Right*) Cartoon representation of D4–D4 homotypic interactions, mediated by two salt bridges between Arg381 and Glu386. Arg381 and Glu386 side chains are shown with sticks, and hydrogen bonds are shown as dashes. (*B*, *Left*) Surface representation of Fab19–KIT$_{D4-5}$ complex, with the same color code as in Fig. 1. Residues Arg381 and Glu386, which mediate D4–D4 homotypic interactions, are indicated by arrows. (*B*, *Right*) Close-up view of the interactions between Arg381 and CDR L2 of Fab19; cartoon representation. Side chains for Arg381, Glu386 (D4), Tyr49 (light chain), and main chain of Leu54 (light chain) are shown with sticks, and hydrogen bonds are shown as dashes.

Table 1. Antibody binding kinetics to KIT D4-D5

Fab	K_a, 1/Ms	K_d, 1/s	K_d, M
KTN37	$(1.5 \pm 0.4) \times 10^{7}$	$(3.6 \pm 0.5) \times 10^{-3}$	$(2.5 \pm 0.3) \times 10^{-10}$
Fab19	$(1.0 \pm 0.7) \times 10^{6}$	$(6.6 \pm 0.2) \times 10^{-4}$	$(6.3 \pm 0.5) \times 10^{-10}$
Fab12I	$(1.4 \pm 0.3) \times 10^{6}$	$(2.7 \pm 0.3) \times 10^{-5}$	$(2.0 \pm 0.6) \times 10^{-11}$
Fab79D	$(2.4 \pm 0.7) \times 10^{6}$	$(1.5 \pm 0.5) \times 10^{-5}$	$(6.4 \pm 0.6) \times 10^{-12}$

EF loop (Fig. 2*A*), are critical for proper ligand dependent receptor activation (7). Analysis of the Fab19–KIT_{D4-5} complex structure revealed that $Arg381^{D4}$ makes contact with CDR L2 of Fab19 (Fig. 2*B*); the $Arg381^{D4}$ side chain makes hydrogen bonds with the side chain of $Tyr49^{L}$ and the main chain of $Leu54^{L}$. In addition, $Tyr101^{H}$ of CDR H3 makes contact with $Thr380^{D4}$ (Fig. S3) of the EF loop, which is involved in mediating D4–D4 homotypic interactions. The structure revealed that contacts between Fab19 and D4 of KIT occluded $Arg381^{D4}$ from forming a salt bridge with Glu-386 of D4 from a neighboring KIT receptor, thereby preventing proper lateral association between membrane-proximal domains. As a consequence, homotypic contacts between the cytoplasmic domains, transphosphorylation and KIT activation were inhibited (as detailed later).

Affinity Maturation of Fab19. To improve the binding affinity of Fab19 to D4, affinity maturation was performed in a two-step process. The first step was performed before solving of the Fab19–KIT_{D4-5} complex structure and involved soft randomization of individual CDRs wherein targeted residues were likely to be kept parental, thereby minimizing the likelihood of changing epitopes during Fab maturation. The four CDRs into which diversity was introduced in library F, CDR L3 and all heavy-chain CDRs, were targeting individually in affinity maturation library design and resulted in the isolation of numerous variants from all four libraries. Variants from the CDR H1 library showed strong improvement over the parental Fab19, and, in particular, Fab12I, estimated to have one of the strongest binding affinity (Fig. S4 *A–C*) and KIT receptor inhibition effect, was chosen for further affinity maturation with the aid of the newly solved Fab19–KIT_{D4-5} complex.

The structure of the Fab19–KIT_{D4-5} complex was used to guide affinity maturation library design after analysis of the antibody–antigen interface revealed that, whereas the heavy chain of Fab19 makes extensive contacts with D4, light-chain interactions were few and weak (Fig. 1*D*). In particular, no contacts were observed between CDR L1 and D4 (Fig. 3*A*). Considering that the light chain makes most of the contact with $Arg381^{D4}$, a residue that is important for formation of D4 homotypic contacts for receptor activation, affinity maturation libraries targeting CDR L1 were designed. Length variation between four and seven residues was incorporated into library design in addition to allowing for possible CDR H1 S31V and/or S33M substitutions found in the parental Fab12I CDR H1 template. Eight unique Fabs (Fab79A–H) were isolated with CDR L1 lengths ranging from four to seven residues, suggesting that increased length allowed additional contacts with D4 (Fig. S4*D*). Interestingly, all clones were found to contain double S31V S33M substitutions in the CDR H1, indicating the importance of these nucleophilic to hydrophobic substitutions (detailed in *SI Appendix*) (Fig. S9).

Binding of Anti-D4 Fabs to KIT_{D4-5} Fragment. We used surface plasmon resonance (SPR) analysis to quantitatively characterize the kinetics and dissociation constants of different generations of affinity-matured anti-D4 Fabs (Fab19, Fab12I, and Fab79D). As a control, we used the Fab of the murine antibody KTN37 (as detailed later). Purified KIT_{D4-5} fragment, was covalently attached onto a CM5 biosensor chip and serial dilutions of each Fab were flowed over the biosensor surface to reveal the binding kinetics (Table 1). Values for the association and dissociation rates showed that the initial phage-derived synthetic Fab19 possessed high binding affinity with a K_d value of 0.63 nM, similar to the affinity of the mouse-derived KTN37 Fab, which had a K_d value of 0.25 nM (Table 1). Although Fab19 and KTN37 Fab had similar affinities, the kinetics were very different: KTN37 bound to KIT with a high association rate but relatively fast dissociation rate whereas Fab19 showed slower association and dissociation rates (Fig. S5). In two steps of affinity maturation, improved binding affinity by two orders of magnitude were observed, bringing binding affinity from the subnanomolar (K_d = 0.63 nM for Fab19) to the picomolar range (K_d = 6.4 pM for Fab79D).

Structure of Fab79D–KIT_{D4-5} Complex. To understand how affinity maturation improved the binding properties of Fab79D compared with Fab19 and to confirm that the binding epitope remained unchanged, we performed crystallization of the Fab79D–KIT_{D4-5} complex. The structure was solved by molecular replacement using the Fab19–KIT_{D4-5} complex as a search model. Data collection and refinement statistics are presented in Table S1.

Comparison between individual domains of the two structures of Fab19 and Fab79D in complex with KIT_{D4-5} fragments showed them to be highly similar with the biggest difference in the elbow angle between D4 and D5 and the elbow angle between the variable and constant domains of the Fabs. Superposition of the constant domains of Fab19 and Fab79D and KIT D5 domains within complex structures revealed rmsd values of 0.41 Å and 0.74 Å for Cα residues, respectively. Similarly, variable domains and D4 were not altered significantly, with rmsd values of 0.55 Å for 279 Cα residues of the VL and VH domains and D4 (Fig. 3*B*). As expected, the biggest difference between the two complexes was found in the CDR L1 loop, which was targeted with length diversity during affinity maturation. Fig. 3*B* shows that the L1 loop of Fab79D moved toward the D4 domain within the Fab79D–KIT_{D4-5} complex structure, and, unlike Fab19, made contact with βD of D4 (Fig. 3*C* and Fig. S6); $Arg31^{L}$ and $Asn32^{L}$ of Fab79D were located within hydrogen bonding distance of the main chain of $Pro363^{D4}$ and side chain of $Glu360^{D4}$, respectively. This CDR L1 loop extension, so evident upon complex structure comparison, appears to be responsible for the increased binding affinity of Fab79D toward KIT D4.

KTN37–Murine Anti-D4 mAb. As a positive control in our experiments, we used KTN37 mAb, a monoclonal antibody obtained by immunization of mice with the KIT_{D4-5} fragment. It was shown that KTN37 IgG bound D4 of human KIT with high affinity, and was a very potent antagonist of the KIT receptor (as detailed

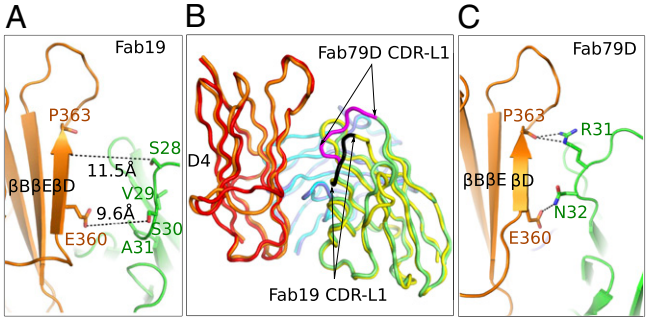

Fig. 3. Comparison of Fab19–KIT_{D4-5} and Fab79D–KIT_{D4-5} complex structures. (*A* and *C*) Cartoon representations of contacts between CDR L1 of Fab19 (*A*) and Fab79D (*C*) and βD of D4. Side chains are shown as sticks, and hydrogen bonds are shown with dashes. (*B*) Structural alignment of VL, VH, and D4 domains from Fab19–KIT_{D4-5} and Fab79D–KIT_{D4-5} structures (ribbon representation). Fab79D complex is colored as follows: D4, orange; VL, green; VH, cyan. Fab19 complex is colored as follows: D4, red; VL, yellow; VH, dark blue. CDRs L1 are highlighted with magenta for Fab79D and with black for Fab19.

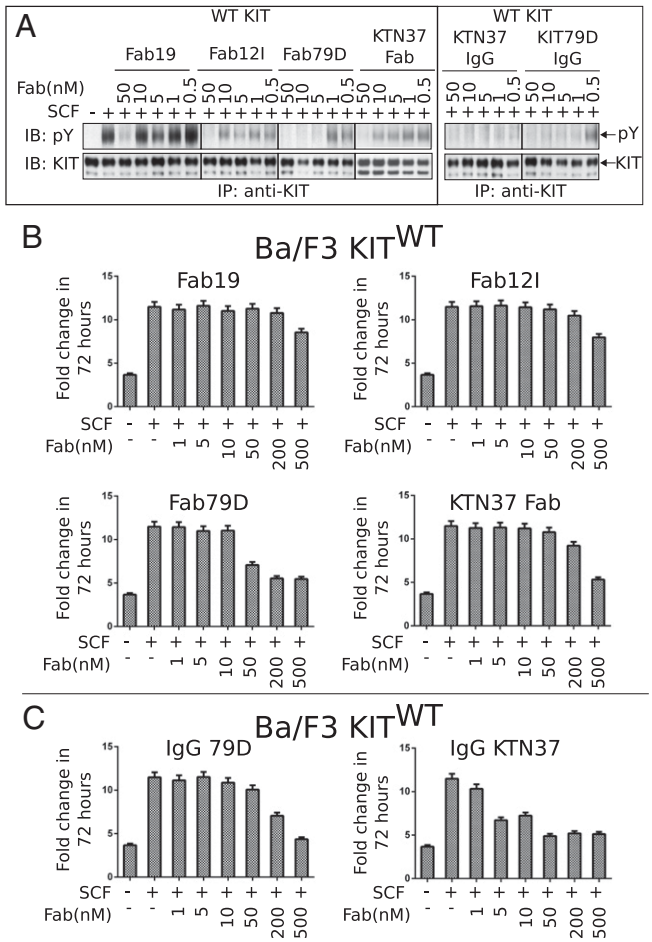

Fig. 4. WT KIT activation is inhibited by anti-D4 antibodies. (*A*) NIH 3T3 cells expressing WT KIT were incubated for 5 h with the indicated concentrations (*Upper*) of Fabs or IgGs following stimulation with 25 ng/mL of SCF for 5 min at 37 °C. Lysates of unstimulated or SCF-stimulated cells were subjected to immunoprecipitation (IP) with anti-KIT antibodies followed by SDS/PAGE and immunoblotting (IB) with anti-KIT or anti-phosphotyrosine (pY) antibodies. (*B* and *C*) Ba/F3 cells expressing WT KIT were plated in six-well plates and grown in the presence of 250 ng/mL SCF and different concentrations as indicated (*Lower*) of Fabs (*B*) or IgGs (*C*). Cell numbers were measured after 72 h relative to 0 h time points.

later). As we were not able to obtain diffraction quality crystals of KTN37 in complex with KIT D4 and D5 fragment, molecular details of the complex could not be obtained. However, to shed light on the binding epitope of KTN37, we compared the KTN37 IgG binding to the ectodomain of KIT from different species (Fig. S7*A*). Our results showed that this mAb was cross-reactive with KIT from human, monkey, dog, and cat, but not mouse or rat. Sequence alignment of D4 of KIT for these six species revealed one major spot with a few residues spread around D4, which are different in the rodent sequences (Fig. S7*B*). We mapped all residue differences onto the D4 structure and found out that most of these residues cover two continuous areas on the surface of D4 (Fig. S8), suggesting that these two regions may represent the binding epitope of KTN37 Fab to D4. It is worth noting that these regions are located right on top of the D4 homotypic contact interface (Fig. S8), and, most likely, binding of KTN37 significantly overlaps with the region essential for mediating D4–D4 homotypic interactions.

KIT Autophosphorylation Is Inhibited by Anti-D4 Antibodies in Living Cells. The crystal structure of Fab19–KIT_{D4-5} and Fab79D–KIT_{D4-5} complexes revealed significant overlap between the Fab binding epitope and the D4–D4 homotypic interface (Fig. S8), important for KIT activation, suggesting that binding of these Fabs likely interferes with KIT receptor autophosphorylation. To test for KIT inhibition, National Institutes of Health (NIH) 3T3 cells expressing WT KIT receptor were incubated for 5 h with varying concentrations of Fabs or IgGs before SCF stimulation. All three generations of synthetic Fabs, together with Fab KTN37, were tested, along with the IgG version of Fab79D (IgG 79D) and IgG KTN37. As predicted from the structure, SCF-stimulated autophosphorylation of KIT was strongly inhibited upon binding of anti-D4 Fabs and IgGs (Fig. 4*A*).

During the two steps of affinity maturation, the inhibitory properties of the anti-D4 Fabs were improved significantly; KIT inhibition by Fab19, the parental synthetic Fab, occurred at 50 nM, whereas the last-generation Fab, Fab79D, inhibited KIT at 5 nM, suggesting that increased affinity correlated to increased KIT inhibition (Fig. 4*A* and Table 1). Consistent with this, Fab12I appears to be more effective at KIT inhibition than Fab19 but weaker than Fab79D.

The bivalent IgG format confers avidity effects to a Fab that are evident upon testing IgG KTN37, whose effectiveness at blocking KIT autophosphorylation could be seen even at 0.5 nM, compared with the 50 nM level required for Fab KTN37 (Fig. 4*A*). Interestingly, much less gain in KIT inhibition from avidity could be seen upon conversion of Fab79D to IgG 79D (5 nM for Fab79D and 1 nM for IgG 79D).

Anti-D4 Antibodies Efficiently Inhibit Proliferation of KIT-Dependent Ba/F3 Cells. We next examined the effect of the Fabs and IgGs on KIT-mediated cell proliferation. We constructed stable Ba/F3 cell lines expressing WT KIT (Ba/F3 KIT^{wt}) or an oncogenic AY502,503 duplication KIT mutant (Ba/F3 $KIT^{AY502,503dup}$). The parental Ba/F3 cells are an IL-3–dependent murine pro-B cells lacking endogenous KIT expression. Upon exogenous WT KIT expression, Ba/F3 cells become dependent on SCF stimulation of these cells. Moreover, expression of constitutively active KIT (such as the AY502,503 duplication in D5) induces transformation of these cells (20). Incubation of these lines with anti-D4 Fabs and IgGs revealed varying cell proliferation inhibition of the D4 binders that correlated with results seen in the KIT autophosphorylation inhibition experiments (Figs. 4 and 5). Like in the inhibition of KIT autophosphorylation experiment, Fab19 could inhibit Ba/F3 KIT^{wt} cell proliferation only at the highest concentration (500 nM), whereas subsequent generations of anti-D4 Fab showed significant improvements to phosphorylation and proliferation inhibition; indeed, Fab79D showed significantly improved inhibitory properties that could inhibit cell growth at 50 nM. KTN37 Fab showed a relatively weak inhibitory effect (200 nM); however, avidity effects contributed significantly upon testing of IgG KTN37, whereupon cell proliferation inhibition could be seen at 1 nM. Conversely, conversion of Fab79D to IgG 79D led to decreased efficacy in cell proliferation assays.

As with the Ba/F3 KIT^{wt} cells overexpressing WT KIT, significant improvements to cell proliferation inhibition of unstimulated Ba/F3 $KIT^{AY502-3dup}$ could also be seen with successive generations of affinity-matured Fabs (Fig. 5). As observed with Ba/F3 $KIT^{AY502-3dup}$ cells, Fab79D (5 nM) proved to be a more effective inhibitor than Fab KTN37 (50 nM); however, IgG KTN37 (1 nM) showed marked improvement whereas the efficacy of IgG 79D (10 nM) was less than that of Fab79D (5 nM). Although IgG KTN37 was a more sensitive cell proliferation inhibitor, able to inhibit proliferation of Ba/F3 $KIT^{AY502-3dup}$ at concentrations lower than that of IgG 79D, overall levels of proliferation were lower in IgG 79D-treated cells than in those treated with IgG KTN37, revealing IgG 79D potency in inhibition of cell proliferation (Fig. 5).

Discussion

Tyrosine kinase inhibitors have been applied successfully in the clinic for treating patients with cancer whose tumors were driven by activated RTKs. Indeed, Gleevec and Sutent have been successfully

BIOCHEMISTRY

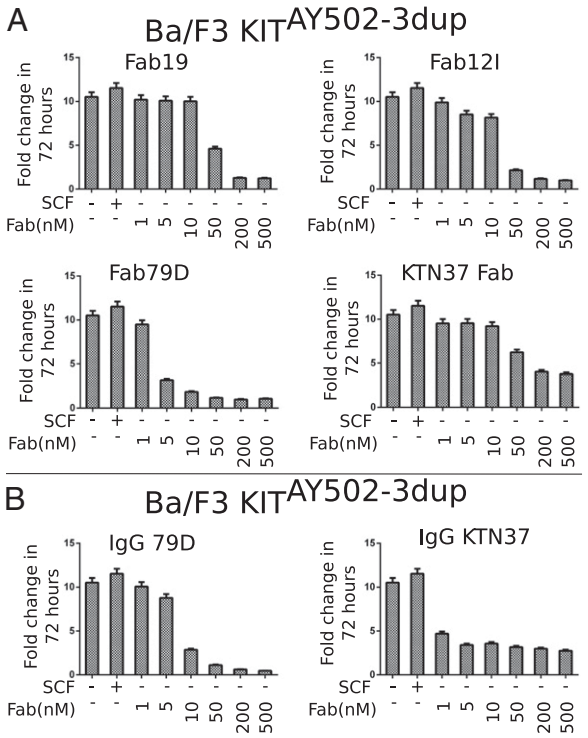

Fig. 5. Proliferation of Ba/F3 cells expressing A502,Y503 duplication oncogenic KIT mutant is inhibited by anti-D4 antibodies. Ba/F3 cells expressing the dupA502,Y503 KIT mutant were plated in six-well plates. Cells were grown in the presence of different concentrations of Fabs (*A*) or IgGs (*B*) in the absence of IL-3 or SCF (as indicated). Fold increase of cell number was measured after 72 h.

developed as important therapeutic options for the treatment of GIST driven by activated KIT (14). Although most patients with KIT-driven GIST respond well when treated with tyrosine kinase inhibitors, sometimes with several years of remission, eventually most cancers relapse because of drug resistance (13, 14). An alternative and complementary approach is to use therapeutic monoclonal antibodies that target the extracellular region of KIT, including mutants that become resistant to tyrosine kinase inhibitors. Moreover, recent advances in the generation of potent and selective toxin conjugates of RTKs may provide an opportunity to actually kill the tumor cells and eliminate the tumor entirely. In this report, we present a step toward accomplishing this goal.

Rational design of a drug that targets the extracellular region of KIT became possible upon solving of the crystal structure and elucidating the mechanism of ligand-induced or oncogenic KIT activation. Crystal structures of the extracellular regions of KIT before and after ligand stimulation (7) strongly emphasized the role of membrane-proximal domain homotypic interactions in receptor activation. Upon ligand binding, the weak homotypic interactions between membrane proximal D4 and D5 allow precise positioning of the two C-terminal regions of the receptor ectodomains in a manner and distance important for positioning of the TM domains in the correct orientation that enable activation of the cytoplasmic tyrosine kinase domain (21–24). Moreover, disruption of homotypic contacts in the membrane-proximal domains of KIT (7), PDGF receptor (22) and VEGF receptor 2 (21) strongly impairs receptor activation. The importance of these domains in activation strongly suggested specific antagonists to the KIT receptor could be generated through membrane proximal domain targeting. Specificity in drug design can be achieved through antibodies that bind with high affinity to their target in a manner necessary to avoid unwanted side effects caused by off-target interactions. Indeed, it was shown previously (25) that monoclonal antibodies against D4 domain of KIT can inhibit receptor activation. Furthermore, the advent of fully human synthetic antibody libraries allows rapid selection of binders specific to their target, coupled with an ability to affinity-mature initially isolated variants for desired attributes such as increased affinity and specificity (18). Here we describe the isolation and maturation of an antibody directed against KIT D4 that strongly impairs receptor activation and cell proliferation to a level that could be potentially used in cancer therapy.

We combined phage display with structural guidance to develop anti-KIT antibodies that hold therapeutic promise. Structural analysis of the Fab19–KIT_{D4-5} complex allowed suboptimal contacts to be determined, thereby permitting facile and focused affinity maturation library design. Indeed, structural analysis revealed that most contacts were mediated by the heavy chain of Fab19, whereas contacts between the light chain and D4 of KIT were crucial for inhibition of KIT receptor. Considering the importance of the light chain contribution to KIT inhibition, affinity maturation libraries were directed toward CDR-L1, lacking any contact between parental Fab19 and KIT D4, that included length variation in attempt to create contacts. This structure-guided strategy proved successful, as significant improvement to inhibitory properties of the final variant (Fab79D) could be seen, especially compared with those of the affinity-matured variant isolated in the absence of structural information (Fab12I). The crystal structures of these inhibitory Fabs in complex with KIT_{D4-5} revealed clear steric blocking of homotypic contacts between the membrane proximal domains of KIT by the Fabs that led to inhibition of receptor autophosphorylation and activation. Considering the conservation of the mechanism of activation of RTKs and the central role played by homotypic contacts between membrane proximal regions in RTK activation similar strategies could be applied to design inhibitors of most, if not all, RTKs.

Despite the affinity of the designed Fab fragment, Fab 79D, being nearly twofold higher than that of Fab KTN37, it was surprising to see such pronounced inhibition by IgG KTN37. Because of the fast association and dissociation rates of Fab KTN37, which result in relatively low KIT binding affinity, a pronounced increase in the binding affinity and inhibitory capacity of IgG KTN37 is achieved by the strong impact of increased valency resulting from an avidity effect. By contrast, the high binding affinity of Fab 79D is primarily caused by the very slow dissociation rate of the monovalent 79D antibody toward KIT binding, and therefore the impact of increased valency (avidity effect) on the binding and inhibitory capacity of IgG 79D toward KIT is rather minimal. Although the two antibodies use different mechanisms for KIT binding, each antibody binds to KIT with high affinity and exerts strong inhibition of KIT activity and function. Comparison of the binding properties of KTN37 to KIT from different species suggests that the binding epitope of Fab KTN37 lies directly on top of the region responsible for mediating the D4–D4 homotypic contacts. However, in the absence of structural information about the exact contact region of Fab KTN37 with KIT D4, it is impossible to compare the exact molecular mechanism of inhibition of the two antibodies. Both antibodies, IgG 79D and IgG KTN37, inhibit proliferation of Ba/F3 cells expressing WT KIT or an oncogenic mutant located in D5 (exon 9) associated with GIST. These two antibodies affect proliferation at nanomolar concentrations and can therefore potentially be used for anticancer therapy and may help to overcome resistance that frequently occurs in patients treated with tyrosine kinase inhibitors. Recent studies have shown that, although mutations to KIT exon 11 (JM domain) are highly sensitive to Gleevec, sensitivity of KIT exon 9 mutants (D5) is at least 10 times lower (14). It is thus not surprising that patients with exon 11 mutations have significantly better disease-free progression and survival than patients with mutations in exon 9, and has led to the idea that resistance to the drug might be caused by subtherapeutic Gleevec dosing in patients with a mutation to KIT exon 9 (13, 14). To address this insensitivity

and resistance to Gleevec, the antibodies developed in the present study have the potential to be used as specific inhibitors of KIT exon 9 mutants. Furthermore, these antibodies can be used in combination with tyrosine kinase inhibitors to allow the use of lower doses to delay or prevent the occurrence of resistance. Finally, the advances in development of potent and selective toxin conjugates may provide an opportunity to develop anti-KIT toxin conjugates that will kill and eliminate the tumor entirely. Here we present a step toward reaching this goal.

Materials and Methods

Proteins Expression and Purification. Soluble KIT_{D4-5} fragment (amino acids 308–514) was expressed in baculovirus Sf9 cells and purified by affinity, size-exclusion, and anion exchange chromatography. All Fab fragments were expressed in *Escherichia coli* and purified by affinity and cation-exchange chromatography. Further details are provided in *SI Materials and Methods*.

Crystallization and Data Collection. Fab19–KIT_{D4-5} and Fab79D–KIT_{D4-5} complexes were crystallized by hanging-drop vapor diffusion methods at 21 °C. Single crystals for both complexes were obtained by macroseeding. For crystallization of Fab19–KIT_{D4-5}, crystallization buffer containing 13% PEG 3350, 0.5 M $MgCl_2$, and 0.1 M Tris·HCl, pH 9.0, was mixed with equal volume (0.6 μL) of protein solution (7 mg/mL). Single crystals were dehydrated by transferring into cryoprotectant solution containing 22% PEG 3350, 0.5 M $MgCl_2$, 0.1 M Tris·HCl, pH 9.0, and 30% ethylene glycol, and were incubated over the reservoir of this buffer for 2 to 3 d. Crystals were flash-frozen in cryoprotectant solution. Crystals of Fab79D–KIT_{D4-5} were obtained by mixing crystallization buffer containing 20% to 24% PEG 400 and 0.1 M Tris·HCl, pH 8.2, with protein sample (6.5 mg/mL). Crystals were flash frozen in the reservoir solution supplemented with PEG 400 up to 35%. X-ray diffraction data were collected at the X25 beamline of National Synchrotron Light Source, Brookhaven National Laboratory. Data collection statistics are summarized in Table S1.

The structures of Fab19–KIT_{D4-5} and Fab79D–KIT_{D4-5} complexes were solved by molecular replacement using the PHASER program (26) under the CCP4 software suite (27) (*SI Appendix*).

Phage Display Selection and Characterization. Phage pools consisting of a phage-displayed synthetic antibody library (library F) were cycled through five rounds of selections by using KIT_{D4-5} immobilized on 96-well MaxiSorp immunoplates (Thermo Scientific) as antigen, as described previously (18). Culture supernatants of 96 clones from each of rounds four and five grown in 96-well format were used directly in phage ELISAs to identify clones binding KIT specifically (using BSA as a negative control). KIT-specific clones were subjected to DNA sequence analysis. Unique clones were subjected to competitive ELISAs that allow for affinity estimation and rank ordering among clones.

Fab Affinity Maturation. KIT affinity maturation libraries were constructed as described previously (19). Briefly, affinity-maturation libraries targeting CDR-H1 were constructed by introducing TAA stop codons into CDR-H1 of phagemid Fab19. The resulting phagemid was used as a template for a mutagenesis reaction that replaced stop codons in CDR-H1 with oligonucleotides mixed in a 70%:10%:10%:10% ratio whereby parental nucleotides were represented at 70% and the remaining nucleotides at 10%. In this manner (soft randomization), targeted residues were biased toward parental but still allowed all 19 possible substitutions.

Cell Culture and Ba/F3 Proliferation Assay. NIH 3T3 cells stably expressing WT-KIT were previously described (7). Further details are provided in *SI Materials and Methods*. Ba/F3 cells were grown in RPMI medium 1640 supplemented with 10% of FBS and 10 ng/mL recombinant murine IL-3. WT and A502,Y503 duplication KIT mutant were cloned into pMSCVpuro vector and transfected into Ba/F3 cells by using electroporation. Stable cell lines expressing WT or mutant KIT were selected in the presence of puromycin and IL-3. After establishing stable cell lines, IL-3 was withdrawn and cells expressing WT KIT were supplemented with 250 nM SCF.

Ba/F3 cells expressing WT or mutant KIT were plated in six-well plates at 400,000 per well in 2 mL media at day 0. Fab or IgG were added to each well at specified concentrations. At 72 h later, cell number was determined by using a Scepter Handheld Automated Cell Counter. Cell number increase is expressed as fold change compared with day 0.

ACKNOWLEDGMENTS. We thank all members of the laboratory of J.S. for valuable discussions and critical comments; the Keck Biophysics facility at Yale University and Ewa Folta-Stogniew particularly for assistance with SPR analysis; and the staff of National Synchrotron Light Source X25, X29A and X6A beamlines. This work was supported by a grant from Kolltan (to I.L.). The T100 Biacore instrumentation was supported by NIH Award S10RR026992-0110.

1. Zhang Z, Zhang R, Joachimiak A, Schlessinger J, Kong XP (2000) Crystal structure of human stem cell factor: Implication for stem cell factor receptor dimerization and activation. *Proc Natl Acad Sci USA* 97(14):7732–7737.
2. Jiang X, et al. (2000) Structure of the active core of human stem cell factor and analysis of binding to its receptor kit. *EMBO J* 19(13):3192–3203.
3. Fleischman RA (1993) From white spots to stem cells: The role of the Kit receptor in mammalian development. *Trends Genet* 9(8):285–290.
4. Huizinga JD, et al. (1995) W/kit gene required for interstitial cells of Cajal and for intestinal pacemaker activity. *Nature* 373(6512):347–349.
5. Lemmon MA, Schlessinger J (2010) Cell signaling by receptor tyrosine kinases. *Cell* 141(7):1117–1134.
6. Roskoski R, Jr. (2005) Signaling by Kit protein-tyrosine kinase—the stem cell factor receptor. *Biochem Biophys Res Commun* 337(1):1–13.
7. Yuzawa S, et al. (2007) Structural basis for activation of the receptor tyrosine kinase KIT by stem cell factor. *Cell* 130(2):323–334.
8. Mol CD, et al. (2004) Structural basis for the autoinhibition and STI-571 inhibition of c-Kit tyrosine kinase. *J Biol Chem* 279(30):31655–31663.
9. Mol CD, et al. (2003) Structure of a c-kit product complex reveals the basis for kinase transactivation. *J Biol Chem* 278(34):31461–31464.
10. Schlessinger J (2000) Cell signaling by receptor tyrosine kinases. *Cell* 103(2):211–225.
11. Lemmon MA, Pinchasi D, Zhou M, Lax I, Schlessinger J (1997) Kit receptor dimerization is driven by bivalent binding of stem cell factor. *J Biol Chem* 272(10):6311–6317.
12. Liu H, Chen X, Focia PJ, He X (2007) Structural basis for stem cell factor-KIT signaling and activation of class III receptor tyrosine kinases. *EMBO J* 26(3):891–901.
13. Ashman LK, Griffith R (2013) Therapeutic targeting of c-KIT in cancer. *Expert Opin Investig Drugs* 22(1):103–115.
14. Corless CL, Barnett CM, Heinrich MC (2011) Gastrointestinal stromal tumours: Origin and molecular oncology. *Nat Rev Cancer* 11(12):865–878.
15. Gajiwala KS, et al. (2009) KIT kinase mutants show unique mechanisms of drug resistance to imatinib and sunitinib in gastrointestinal stromal tumor patients. *Proc Natl Acad Sci USA* 106(5):1542–1547.
16. Swain SM, et al. (2013) Pertuzumab, trastuzumab, and docetaxel for HER2-positive metastatic breast cancer (CLEOPATRA study): Overall survival results from a randomised, double-blind, placebo-controlled, phase 3 study. *Lancet Oncol* 14(6):461–471.
17. Baselga J, et al.; CLEOPATRA Study Group (2012) Pertuzumab plus trastuzumab plus docetaxel for metastatic breast cancer. *N Engl J Med* 366(2):109–119.
18. Persson H, et al. (2013) CDR-H3 diversity is not required for antigen recognition by synthetic antibodies. *J Mol Biol* 425(4):803–811.
19. Nelson B, Sidhu SS (2012) Synthetic antibody libraries. *Methods Mol Biol* 899:27–41.
20. Guo T, et al. (2007) Sorafenib inhibits the imatinib-resistant KITT670I gatekeeper mutation in gastrointestinal stromal tumor. *Clin Cancer Res* 13(16):4874–4881.
21. Yang Y, Xie P, Opatowsky Y, Schlessinger J (2010) Direct contacts between extracellular membrane-proximal domains are required for VEGF receptor activation and cell signaling. *Proc Natl Acad Sci USA* 107(5):1906–1911.
22. Yang Y, Yuzawa S, Schlessinger J (2008) Contacts between membrane proximal regions of the PDGF receptor ectodomain are required for receptor activation but not for receptor dimerization. *Proc Natl Acad Sci USA* 105(22):7681–7686.
23. Arkhipov A, et al. (2013) Architecture and membrane interactions of the EGF receptor. *Cell* 152(3):557–569.
24. Endres NF, et al. (2013) Conformational coupling across the plasma membrane in activation of the EGF receptor. *Cell* 152(3):543–556.
25. Blechman JM, et al. (1995) The fourth immunoglobulin domain of the stem cell factor receptor couples ligand binding to signal transduction. *Cell* 80(1):103–113.
26. McCoy AJ, et al. (2007) Phaser crystallographic software. *J Appl Cryst* 40(pt 4): 658–674.
27. Winn MD, et al. (2011) Overview of the CCP4 suite and current developments. *Acta Crystallogr D Biol Crystallogr* 67(pt 4):235–242.

Supporting Information

Reshetnyak et al. 10.1073/pnas.1317118110

SI Appendix

Detailed Information About Fab19–KIT D4 Interface. The overall shape complementarity (SC) parameter for the Fab19–KIT_{D4-5} (recombinant KIT D4 and D5 fragment) interface was 0.70, slightly higher than observed typically (0.65–0.68) for an antibody–antigen binding interface (1). A higher SC parameter correlates to higher affinity or more convex shape of the antibody–antigen interface; indeed, similar or even higher SC values (in the range from 0.7 to 0.75) have been observed for therapeutic antibody–antigen complexes such as cetuximab (2), trastuzumab (3), and pertuzumab (4).

The AA′ loop of D4 (residues $Pro317^{D4}$–$Asn320^{D4}$, where D4 stands for the D4 domain of KIT) was buried in the cavity created by the heavy chain complementarity-determining regions (CDRs) H1 and H2 (Fig. S3 *A* and *B*). In particular, CDR H2 created a pronounced hydrophobic pocket ($Tyr52^{H}$, $Tyr54^{H}$, $Ser55^{H}$, and $Tyr57^{H}$, with H representing heavy chain) that interacted with $Pro317^{D4}$, $Met318^{D4}$, and $Asn320^{D4}$ of the AA′ loop of the D4 (Figs. S2 and S3*B*). $Ser30^{H}$ and $Ser31^{H}$ of the CDR H1 made van der Waals contacts with $Ile319^{D4}$ and glycosylated $Asn320^{D4}$; $Ser30^{H}$ was also located within hydrogen bond distance from the main chain of $Asn320^{D4}$ (Figs. S2 and S3*A*). $Tyr32^{H}$ from CDR H1 also interacted with the A′B loop of D4 ($Asn330^{D4}$ and $Glu329^{D4}$) through van der Waals interactions and hydrogen bonding with the main chain of $Asn330^{D4}$. CDR H2 makes additional interactions with βB ($Tyr52^{H}$ and $Tyr57^{H}$ interact with $Ile334^{D4}$ and $Glu336^{D4}$, respectively), βE ($Tyr57^{H}$ makes a hydrogen bond with $Arg372^{D4}$), and DE loop ($Tyr59^{H}$ makes van der Waals contacts with $Lys364^{D4}$). CDR H3 makes extensive polar and hydrophobic contacts with βB, βE, βD, and A′B and EF loops of D4 (Figs. S2 and S3*C*). Moreover, $Tyr101^{H}$ of CDR H3 made a π–π staking with $His378^{D4}$ while also interacting with $Thr380^{D4}$, $Lys358^{D4}$, and $Asp332^{D4}$. $His102^{H}$ and $Val100^{H}$ of CDR H3 were additional key residues, making contact with $Glu360^{D4}$, $Glu376^{D4}$, $His378^{D4}$, and $Val331^{D4}$, $Asp332^{D4}$. $Arg98^{H}$, located at the base of CDR H3, formed a salt bridge with $Glu329^{D4}$. Finally, CDRs L2 ($Tyr49^{L}$ and $Leu54^{L}$) and L3 ($Trp91^{L}$, $Val93^{L}$, and $His94^{L}$) of the light chain were involved in interactions with βD ($Tyr362^{D4}$), DE ($Glu366^{D4}$), and EF ($Arg381^{D4}$) loops of the D4 (Figs. 2*B*, S2, and S3*D*).

Impact of S31V and S33M Substitutions. Fab12I was among the strongest Fab binders selected during first generation of affinity maturation and contained two substitutions in CDR H1: S31/V and S33/M. The same substitutions in CDR H1 were permitted during the second generation of structurally guided affinity maturation targeting CDR L1 and resulting in the isolation of Fabs all containing both substitutions (S31/V and S33/M). Analysis using structural alignments of CDR H1 from structures of Fab19 and Fab79D complexes is depicted in Fig. S9, with Fab19 colored in cyan and Fab79D in blue. Substitution of S31/V increased hydrophobicity of this residue and allowed additional van der Waals interactions with $Val323^{D4}$, explaining the increased affinity to KIT D4. Surprisingly, no contacts between $Ser33^{H}$ (for Fab19) or $Met33^{H}$ (Fab79D) and KIT D4 were found. We propose that substitution of Ser33 to Met stabilizes conformation of CDR H1 by additional hydrophobic contacts between $Met33^{H}$ and $Tyr51^{H}$ (Fig. S9). This conformation of CDR H1 would be poised for binding to KIT D4 and would not require additional energy for stabilization upon binding as in the case of Fab19.

To understand the role of individual CDR H1 mutations, we generated Fab19–S31V and Fab19–S33M single mutants to analyze their binding affinities to the KIT_{D4-5} fragment. Both mutants demonstrated increased binding affinities compared with those of parental Fab19:

Fab	K_a, 1/Ms	K_d, 1/s	K_d, M
KIT19	$(1.0 \pm 0.7) \times 10^{6}$	$(6.6 \pm 0.2) \times 10^{-4}$	$(6.3 \pm 0.5) \times 10^{-10}$
KIT19-S31V	$(9.5 \pm 0.3) \times 10^{5}$	$(3.2 \pm 0.2) \times 10^{-4}$	$(3.4 \pm 0.2) \times 10^{-10}$
KIT19S33M	$(1.2 \pm 0.2) \times 10^{6}$	$(2.7 \pm 0.2) \times 10^{-4}$	$(2.4 \pm 0.2) \times 10^{-10}$

SI Materials and Methods

Expression and Purification of KIT_{D4-5}. Soluble KIT_{D4-5} fragments were expressed in Sf9 insect cells according to the Bac-to-Bac instruction manual (Invitrogen), using Grace insect medium supplemented with 10% heat-inactivated FBS. At 72 h after infection, cells were harvested by centrifugation at 500 × *g* and lysed by sonication on ice in lysis buffer (100 mM potassium phosphate buffer, pH 8.0, 300 mM NaCl, 25 mM imidazole, 10% glycerol, and 1% NDP-40). Crude lysate was cleared by centrifugation at 125,000 × *g* and filtered through 0.65-μm PVDF filter, and was applied to Ni-NTA agarose (Qiagen). Ni-NTA beads were washed with 50 column volumes (CVs) of wash buffer (100 mM potassium phosphate buffer, pH 8.0, 300 mM NaCl, 25 mM imidazole, 10% glycerol) and eluted with elution buffer (100 mM potassium phosphate buffer, pH 8.0, 300 mM NaCl, 250 mM imidazole, 10% glycerol). Eluted proteins were injected onto a HiLoad 26/600 Superdex 200 (GE Healthcare) equilibrated with 10 mM Tris, pH 8.0, 200 mM NaCl. Fractions corresponding to KIT_{D4-5} fragment were combined and concentrated by using a Vivaspin concentrator (GE Healthcare) with a molecular weight cut-off of 10 kDa. The concentrated sample was deglycosylated with recombinant endoglycosidase F1 at a final 1:50 wt/wt ratio, for 12 h at room temperature. Simultaneously the 6His tag was cleaved by adding 1:100 wt/wt ratio of recombinant tobacco etch virus (TEV) protease that preceded deglycosylation and TEV treatment of KIT_{D4-5} that was purified by anion exchange chromatography at 16/10 MonoQ column using 40 CV gradient from buffer A (10 mM Bis-Tris, pH 6.5) to 50% of buffer B (10 mM Bis-Tris, pH 6.5, 1 M NaCl). Fractions containing KIT_{D4-5} fragment were combined and concentrated. For surface plasmon resonance (SPR) analysis, the buffer of the KIT_{D4-5} was additionally exchanged to an HSP-P+ buffer using a Superdex 75 10/300 GL (GE Healthcare).

Fab Expression and Purification. Synthetic codon optimized bicistronic DNA of KTN37 Fab was cloned into pET26 vector using NcoI and SalI/XhoI restriction sites. A His-tag was introduced into the C terminus of heavy chain of KTN37 Fab. Phagemids as described by Nelson and Sidhu (5) were used for Fab19, Fab12I, and Fab79D expression. BL21(DE3) was transformed with appropriate phagemid or pET26-KTN37 and single colony was used for expression in Terrific Broth (TB) media by using the autoinduction protocol (6). After overnight expression at 22 °C, cells were harvested and flash-frozen in appropriate lysis buffer containing 1×

TBS (Fab19, Fab12I, and Fab79D) or 100 mM potassium phosphate buffer, pH 8.0, 300 mM NaCl, 25 mM imidazole, 10% glycerol (KTN37 Fab). Cells were lysed by using a French press, and crude lysate was cleared by centrifugation at 40,000 × *g* and filtration through a 0.65-μm PVDF filter. Cleared lysates of Fab19, Fab12I, or Fab79D were applied to Protein A Sepharose (Invitrogen) equilibrated with 1× TBS buffer. Unbound proteins were washed out with 50 CVs of 1× TBS buffer. Fabs were eluted with 100 mM glycine-HCl buffer, pH 3.2, and immediately neutralized with 1 M Tris·HCl, pH 8.0, buffer.

Cleared lysate of KTN37 Fab was applied to Ni-NTA agarose (Qiagen). Unbound proteins were washed out with 50 CVs of wash buffer (100 mM potassium phosphate buffer, pH 8.0, 300 mM NaCl, 25 mM imidazole, 10% glycerol). KTN37-Fab was eluted with elution buffer (100 mM potassium phosphate buffer, pH 8.0, 300 mM NaCl, 250 mM imidazole, 10% glycerol) and applied onto a HiLoad 26/600 Superdex 200 equilibrated with 1× TBS. The buffers of all Fab solutions were exchanged to a 10-mM sodium acetate, pH 5.0, buffer by using a HiPrep 26/10 desalting column, and applied to Source S HR 16/10 column equilibrated with the same buffer. Fabs were eluted with 20 CVs gradient from 10 mM sodium acetate, pH 5.0, buffer to 10 mM sodium acetate, pH 5.0, 1 M NaCl. Fractions containing assembled Fabs were neutralized with 1 M Tris·HCl, pH 8.0, and concentrated. For the SPR analysis, the buffers of KIT_{D4-5} was additionally exchanged to an HSP-P+ buffer by using a Superdex 75 10/300 GL (GE Healthcare).

KTN37 and KIT79D Full-Length IgG. DNA fragments encoding variable regions of heavy and light chain of KTN37M were isolated by RT-PCR from the hybridoma cell line expressing KTN37M (M stands for murine). For construction of full-length antibodies, DNA fragment from variable domains of heavy and light chain of KTN37M and KIT79D were subcloned into the antibody cassette vectors, phIgG1 (human IgG1 backbone) and phIgK (human κ backbone), that contain human constant regions, respectively. Mouse heavy-chain signal peptides were added at the N terminus of each construct for secretion. Resulting plasmids encoding heavy and light chains of KTN37C and IgG 79D-H (C stands for murine-human chimera and H stands for full human antibody) were transfected into 293F cells (Invitrogen). After 3 d, the culture media were harvested, applied to Protein A Sepharose and eluted with 0.2 M glycine-HCl (pH 2.7) followed by neutralization by 1 M Tris·HCl (pH 8.0).

Structure Determination and Refinement. For the Fab19–KIT_{D4-5} complex, we collected a native dataset at X25 beamline National Synchrotron Light Source (NSLS). This crystal diffracted to 2.4-Å resolution (Table S1), with unit cell parameters of a = 169.6 Å, b = 49.0 Å, c = 107.0 Å, α = γ = 90°, and β = 122.4° in *C*2 space group. For the Fab79D–KIT_{D4-5} complex, we collected a native dataset at beamline X29A at NSLS. The Fab79D-KIT_{D4-5} complex crystal diffracted to 2.7 Å resolution (Table S1) and had unit cell parameters of a = b = 95.9 Å, c = 322.6 Å, α = γ = 90°, β = 122.4° in space group $P6_522$. The processed datasets for both structures were strongly anisotropic and were corrected for anisotropy using the Diffraction Anisotropy Server at University of California, Los Angeles (http://services.mbi.ucla.edu/anisoscale/) (7).

Fab19–KIT_{D4-5} complex. Matthews coefficient analysis suggested the highest probability of one Fab19–KIT_{D4-5} complex molecule per asymmetric unit. Molecular replacement was conducted using Phaser (8), and the following ensembles used as search models: ensemble 1, Fv region of humanized anti-p185HER2 antibody 4D5 [Protein Data Bank (PDB) ID code 1FVE: chain A, residues 1–104; and chain B, residues 1–122]; ensemble 2, KIT D4 (PDB ID code 2EC8, residues 312–408); ensemble 3, constant domain of the heavy chain of humanized anti-p185HER2 antibody 4D5 (PDB ID code 1FVE, chain B, residues 121–223); ensemble 4, constant domain of the light chain of humanized anti-p185HER2 antibody 4D5 (PDB ID code 1FVE, chain A, residues 110–214); and ensemble 5, KIT D5 (PDB ID code 2EC8, residues 410–504) (9, 10). A single solution was found using this strategy. Standard refinement and model building techniques using Refmac (11) and Coot (12) were then followed. Phenix refine was used for the last stage of refinement (13).

Fab79D–KIT_{D4-5} complex. The structure of Fab79D–KIT_{D4-5} complex was solved by molecular replacement by using Phaser (8). A clear molecular replacement solution was found using the refined Fab19–KIT_{D4-5} complex structure as a search model. The Fab19–KIT_{D4-5} complex structure (from this work) was split into four search models: ensemble 1, variable fragment of Fab19 (chain A residues 3–108 and chain B residues 1–120) and KIT D4 fragment (chain C residues 310–409); ensemble 2, Ch fragment (chain B residues 121–217); ensemble 3, Cl fragment (chain A residues 113–209); and ensemble 4, KIT D4 fragment (chain C residues 410–504). Strong electron density has been seen at the C terminus of the light chain of Fab79D and was assigned to the Flag tag, but because electron density is missing in the linker region between Flag tag and light chain, precise determination of the registry for the Flag tag is impossible. The same refinement strategy as was used for Fab19–KIT_{D4-5} complex structure was used for refinement of Fab79D–KIT_{D4-5} complex structure.

Data collection and refinement statistics for both structures are summarized in Table S1.

Competitive ELISA. Briefly, supernatant from clones grown in 96-well format was incubated for 1 h with specified concentrations of soluble antigen before being applied to KIT_{D4-5} immobilized to Maxisorp immunoplates for 15 min. Signal inhibition was compared with phage incubated in the absence of soluble antigen. Multipoint ELISAs involving normalization of purified phage particles (grown in 30 mL cultures and quantified by using A_{268}) and eight fourfold serial dilutions used for ELISAs were also used to rank variants.

Fab Affinity Maturation. Affinity maturation libraries targeting CDR-L1 were constructed by introducing TAA stop codons into CDR-L1 and CDR-H1 of phagemid Fab19. The resulting phagemid was used for three independent mutagenesis reactions to replace stop codons of CDR-H1 with Fab19 CDR-H1 containing either the double S31VS33M substitution, the S31V single substitution, or the S33M single substitution. CDR-L1 was targeted simultaneously in all three libraries by replacing CDR-L1 stop codons with four to seven NNK codons (representing all 20 aa). The three libraries were mixed together before selections.

SPR Analysis. SPR experiments were performed by using a BiaCore T100 instrument at 25 °C in the HSP-P+ buffer (cat. no. BR-1006-71; GE Healthcare). KIT_{D4-5} fragment (2.5 μg/mL) was immobilized on a CM5 BiaCore sensor chip (GE Healthcare) using standard amine coupling. Optimum coupling was achieved in 10 mM sodium acetate buffer, pH 4.5. Surfaces with three different concentration of immobilized KIT_{D4-5} fragment were obtained by varying contact time (from 50 to 120 s). Non–cross-linked ligand was removed, and unreacted sites were blocked with 1 M ethanolamine, pH 8.5.

Purified Fab analytes at series of threefold dilution concentrations (0.12–10 nM) were flowed simultaneously over three different concentrations of immobilized KIT_{D4-5} and reference surfaces. To obtain a reliable signal-to-noise ratio, a longer dissociation time was used for Fab12I and Fab79D (Fig. S5*B*). Data were analyzed by using the Biacore T100 Evaluation software.

Cell Culture, Immunoprecipitation, and Immunoblotting Experiments. National Institutes of Health 3T3 cells stably expressing WT-KIT were previously described (10). Cells were cultured in DMEM (Invitrogen) containing 10% bovine serum and were starved overnight in serum-free medium before incubation with Fabs and/or

stem cell factor (SCF) stimulation. Cells were incubated with the indicated (Fig. 4*A*) concentrations of Fabs for 5 h, followed by stimulation with SCF. Cells were lysed as previously described (14) and subjected to immunoprecipitation with anti-KIT antibodies (10), followed by immunoblotting with anti-KIT or anti-pY (4G10; Upstate Biotechnology) antibodies.

1. Lawrence MC, Colman PM (1993) Shape complementarity at protein/protein interfaces. *J Mol Biol* 234(4):946–950.
2. Li S, et al. (2005) Structural basis for inhibition of the epidermal growth factor receptor by cetuximab. *Cancer Cell* 7(4):301–311.
3. Cho HS, et al. (2003) Structure of the extracellular region of HER2 alone and in complex with the Herceptin Fab. *Nature* 421(6924):756–760.
4. Franklin MC, et al. (2004) Insights into ErbB signaling from the structure of the ErbB2-pertuzumab complex. *Cancer Cell* 5(4):317–328.
5. Nelson B, Sidhu SS (2012) Synthetic antibody libraries. *Methods Mol Biol* 899:27–41.
6. Studier FW (2005) Protein production by auto-induction in high density shaking cultures. *Protein Expr Purif* 41(1):207–34.
7. Strong M, et al. (2006) Toward the structural genomics of complexes: Crystal structure of a PE/PPE protein complex from Mycobacterium tuberculosis. *Proc Natl Acad Sci USA* 103(21):8060–8065.
8. McCoy AJ, et al. (2007) Phaser crystallographic software. *J Appl Cryst* 40(pt 4):658–674.
9. Eigenbrot C, Randal M, Presta L, Carter P, Kossiakoff AA (1993) X-ray structures of the antigen-binding domains from three variants of humanized anti-p185HER2 antibody 4D5 and comparison with molecular modeling. *J Mol Biol* 229(4):969–995.
10. Yuzawa S, et al. (2007) Structural basis for activation of the receptor tyrosine kinase KIT by stem cell factor. *Cell* 130(2):323–334.
11. Murshudov GN, Vagin AA, Dodson EJ (1997) Refinement of macromolecular structures by the maximum-likelihood method. *Acta Crystallogr D Biol Crystallogr* 53(pt 3):240–255.
12. Emsley P, Lohkamp B, Scott WG, Cowtan K (2010) Features and development of Coot. *Acta Crystallogr D Biol Crystallogr* 66(Pt 4):486–501.
13. Afonine PV, et al. (2012) Towards automated crystallographic structure refinement with phenix.refine. *Acta Crystallogr D Biol Crystallogr* 68(pt 4):352–367.
14. Lax I, et al. (2002) The docking protein FRS2alpha controls a MAP kinase-mediated negative feedback mechanism for signaling by FGF receptors. *Mol Cell* 10(4):709–719.

	L1				L3							H1						H2									H3							
Fab19	S	V	S	S	W	A	V	H	S	L	I	I	S	S	Y	S	M	S	I	Y	P	Y	S	G	Y	T	Y	V	Y	H	A	L	D	Y	W
Library F	S	V	S	S	X	X	X	X	X	PL	FI	IL	YS	YS	YS	YS	IM	YS	I	YS	PS	YS	YS	GS	YS	T	YS	X	X	X	X	X	X	AG	FILM

Fig. S1. Isolation of Fab19 from a naïve synthetic antibody library. CDR sequences of a naive synthetic Fab library and Fab19.

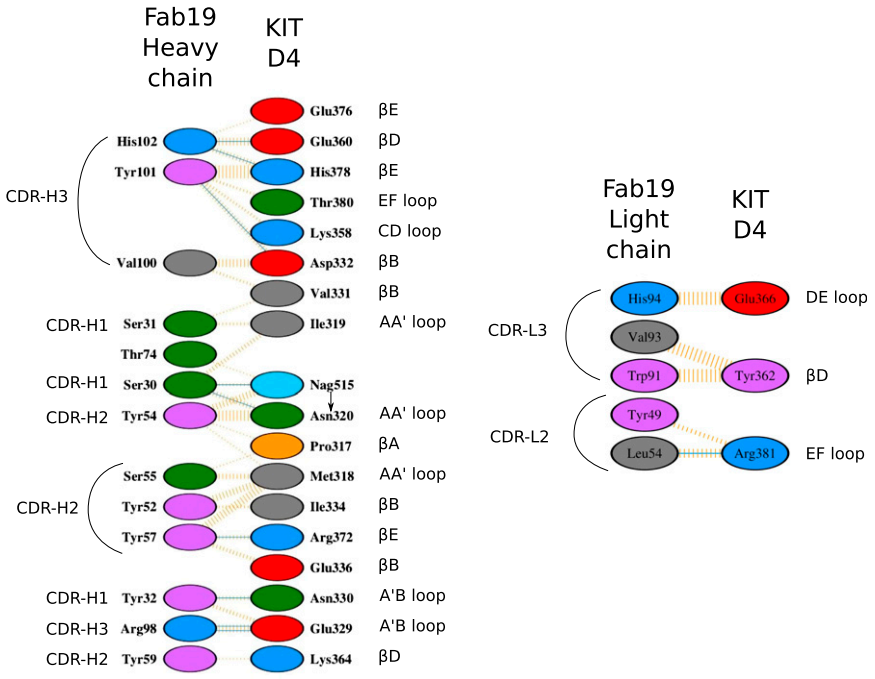

Fig. S2. Diagram of amino acids mediating the interaction between Fab19 and D4 of KIT. Diagrams were generated by using the PDBsum server (1). Amino acids are colored according to their chemical properties; positive in blue, negative in red, neutral in green, aliphatic in gray, and aromatic in purple. Interactions are depicted in blue solid and orange striped lines for hydrogen bonds and nonbonded contacts, respectively. For nonbonded contacts, the thickness of the lines corresponds to the number of contacts.

1. Laskowski RA (2007) Enhancing the functional annotation of PDB structures in PDBsum using key figures extracted from the literature. *Bioinformatics* 23(14):1824–1827.

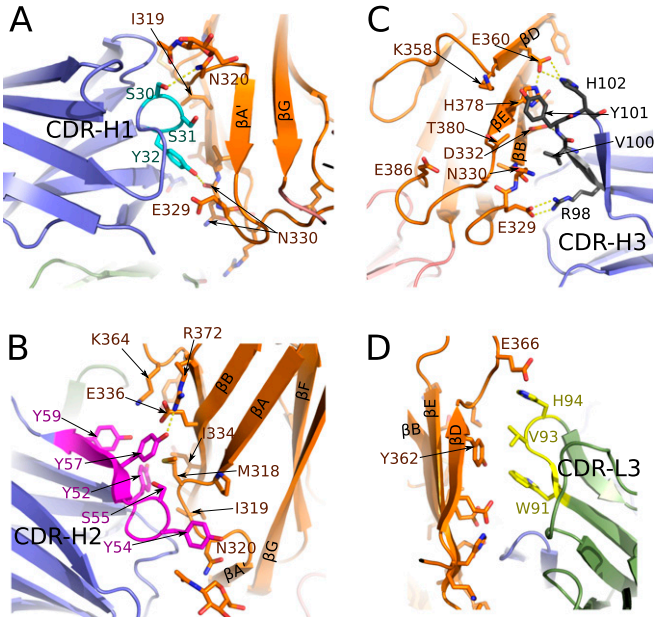

Fig. S3. Fab19–KIT_{D4-5} interface. Detailed view of the interactions between Fab19 and KIT_{D4-5} fragment as a cartoon representation. Side chains mediating interactions are shown with sticks and hydrogen bonds with dashes. General color code is the same as in Fig. 1; CDR H1 (*A*) is in cyan, H2 (*B*) in magenta, H3 (*C*) in gray, and L3 (*D*) in yellow.

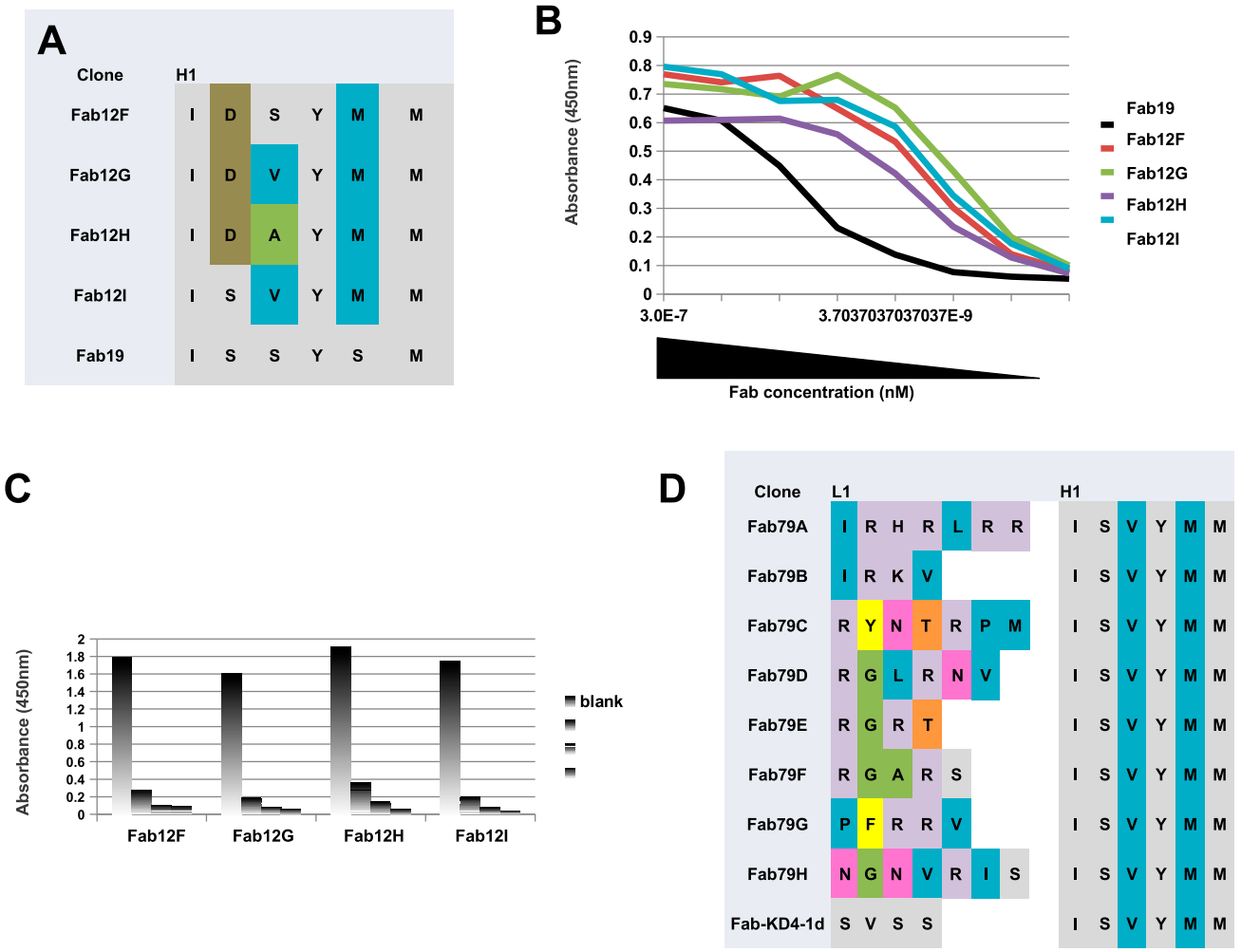

Fig. S4. Isolation and characterization of affinity-mature anti-KIT D4 Fab. (*A*) CDR-H1 sequences of isolated affinity-matured variants. (*B*) Multipoint ELISA to compare affinities of variants using serial dilutions of normalized phage and purified bound antigen. (*C*) Fluid phase competitive ELISA using a combination of phage and purified antigen in solution at specified concentrations that competes with constant concentrations of immobilized antigen to estimate binding affinity of affinity-matured variants to KIT D4. (*D*) CDR-L1 and H1 sequences of Fabs isolated in the second generation of affinity maturation.

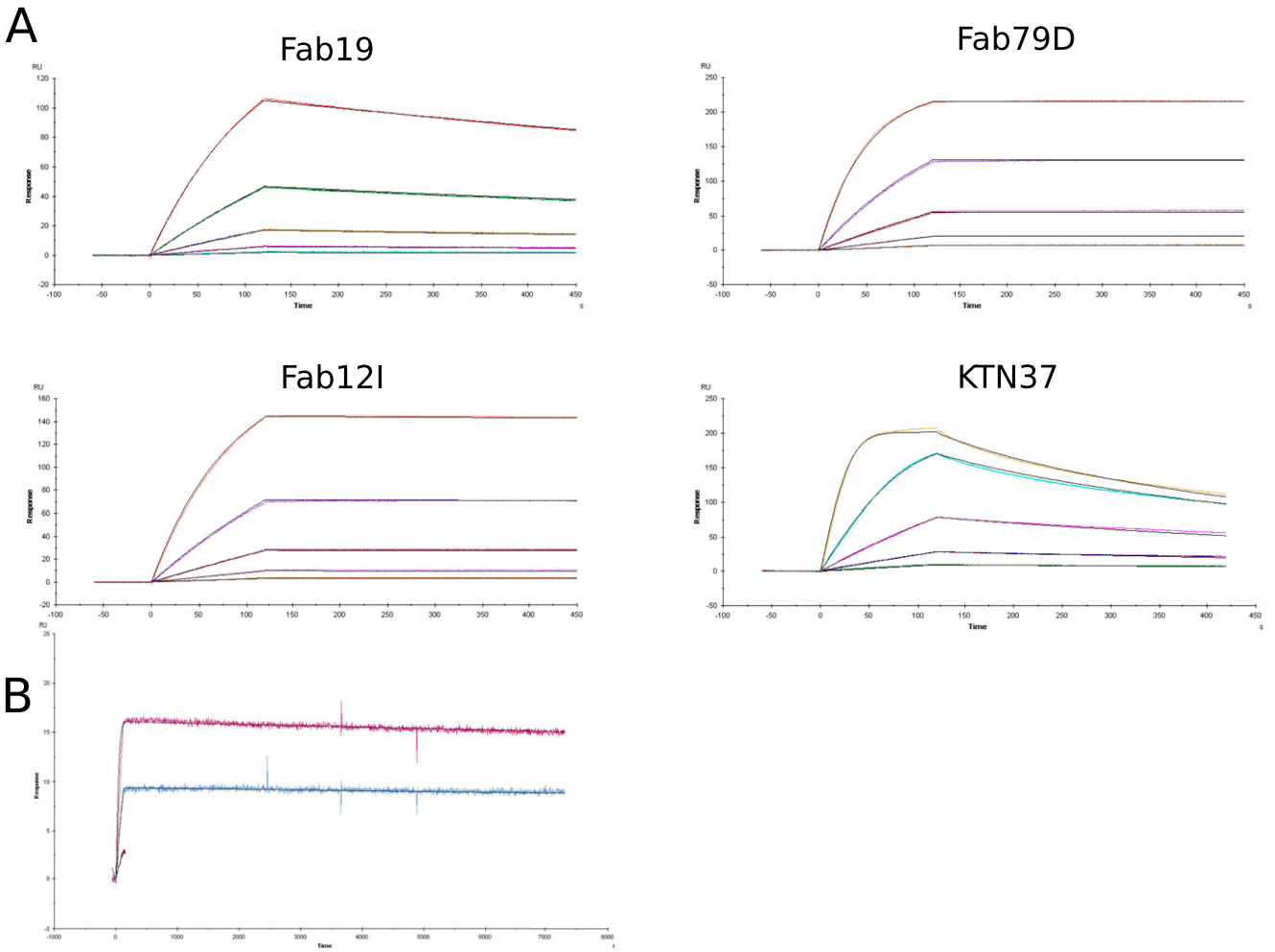

Fig. S5. Comparison of binding kinetics of anti-D4 Fabs to KIT_{D4-5} fragment. SPR analysis of binding of Fab19, Fab12I, Fab79D, and Fab-KTN37 to immobilized KIT_{D4-5} fragment. Fabs in serial dilution (0.12 nM, 0.37 nM, 1.1 nM, 3.3 nM, and 10 nM) were passed over Biosensor surface to which KIT_{D4-5} fragment was covalently coupled. (*A*) Association and dissociation kinetic curves are shown for each Fab. The data were fit into 1:1 Langmuir interaction model (1) (black lines) using Biacore T100 Evaluation software. To get reliable fitting, dissociation times were significantly increased for Fab79D binding (*B*).

1. O'Shannessy DJ, Brigham-Burke M, Soneson KK, Hensley P, Brooks I (1993) Determination of rate and equilibrium binding constants for macromolecular interactions using surface plasmon resonance: Use of nonlinear least squares analysis methods. *Anal Biochem* 212(2):457–468.

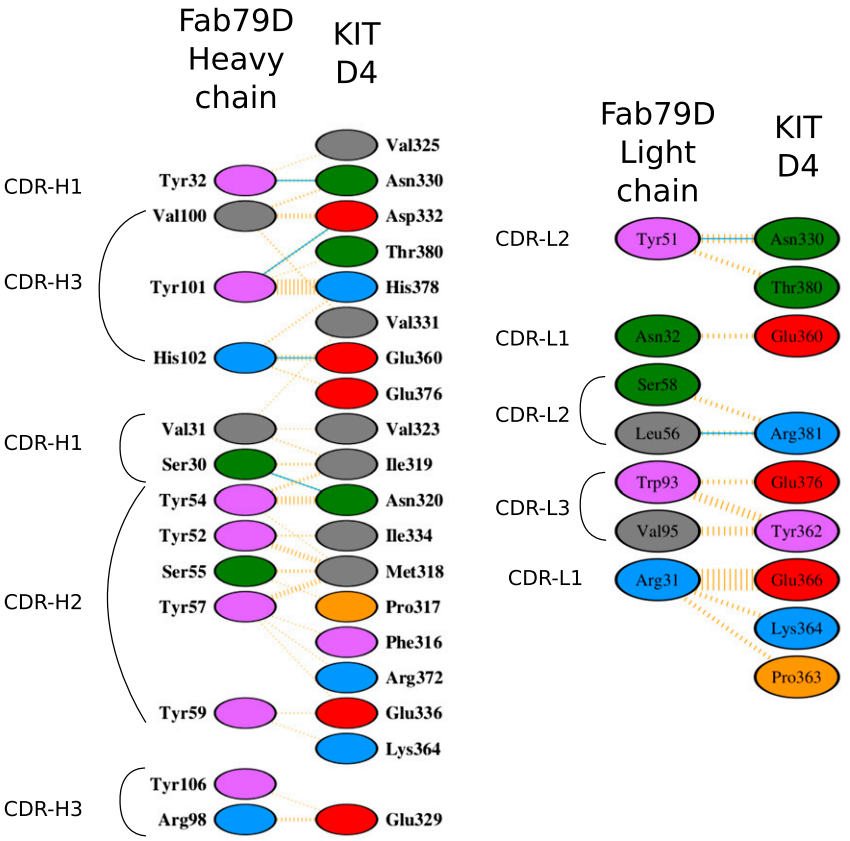

Fig. S6. Diagram of amino acids mediating the interaction between Fab79D and D4 of KIT. Diagrams were generated using the PDBsum server (1). Amino acids are colored according to their chemical properties; positive in blue, negative in red, neutral in green, aliphatic in gray, and aromatic in purple. Interactions are depicted in blue solid and orange striped lines for hydrogen bonds and nonbonded contacts, respectively. For nonbonded contacts, the thickness of the lines corresponds to the number of contacts.

1. Laskowski RA (2007) Enhancing the functional annotation of PDB structures in PDBsum using key figures extracted from the literature. *Bioinformatics* 23(14):1824–1827.

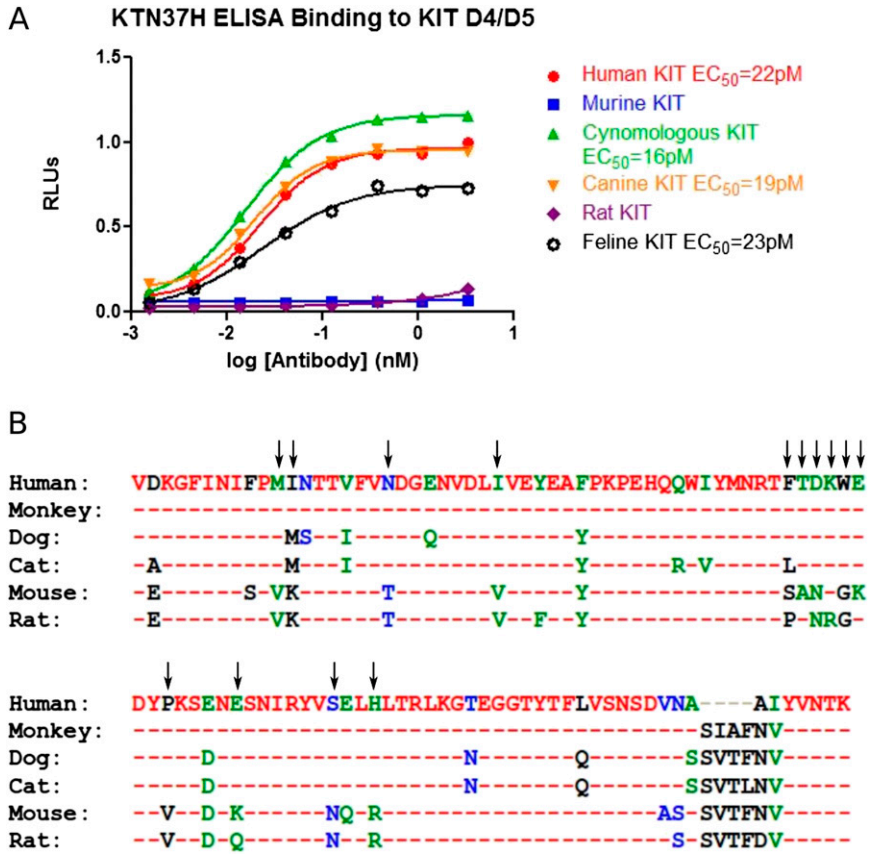

Fig. S7. Binding of KTN37 IgG to KIT_{D4-5} of different species. (*A*) ELISA analysis of binding of KTN37 IgG to KIT_{D4-5} fragment from different species. (*B*) Protein sequence alignment of KIT D4 form different species. Residues different between rodent (do not bind to KTN37 IgG) and other mammal sequences are highlighted with arrows. These residues may represent a region in KIT D4 essential for KTN37 IgG binding.

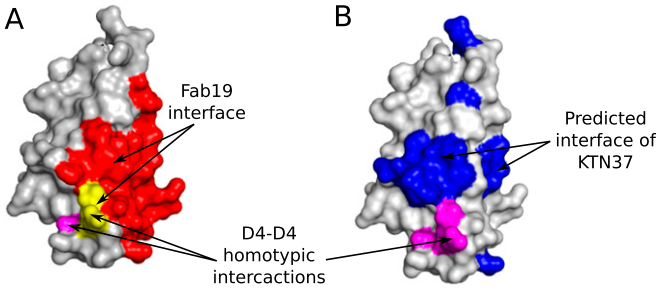

Fig. S8. Interfaces between KIT_{D4} and Fab19 or KTN37. Surface representation of KIT_{D4} fragment. (*A*) Interface between KIT_{D4} and Fab19 and its overlap with D4–D4 homotypic interactions. The surface is colored according to whether it interacts with Fab19 only (red), another D4 during ligand dependent dimerization (magenta), or both (yellow). (*B*) Theoretical interface of KTN37 IgG. Residues potentially involved into KTN37–D4 interactions (Fig. S6) are colored blue; residues involved into D4–D4 homotypic interactions are colored magenta.

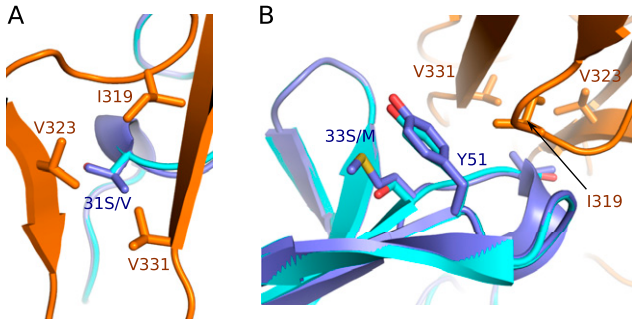

Fig. S9. Superposition of CDR H1 of Fab19 and Fab79D. Cartoon representation of Fab19–KIT_{D4-5} and Fab79D–KIT_{D4-5} structures with side chains are shown with sticks, and variable regions of heavy chains of Fab19 and Fab79D were aligned. Heavy chain of Fab19 is colored cyan; heavy chain of Fab79D is colored blue; KIT D4 is colored orange. (*A*) Interaction of $Ser/Val31^{H}$ with KIT D4 (residues $Ile319^{D4}$, $Van323^{D4}$, and $Val331^{D4}$). (*B*) Substitution of $Ser33^{H}$ (Fab19) to Met (Fab79D) increases hydrophobic interactions with $Tyr51^{H}$ stabilizing conformation of CDR H1 loop.

Table S1. Data collection and refinement statistics

	Fab19-KIT$_{D4-5}$	Fab79D-KIT$_{D4-5}$
X-ray source	NSLS X25	NSLS X29A
No. of crystals	1	1
Wavelength, Å	1.1000	1.0750
Unit cell dimensions	*C2*	*P6$_5$22*
a, Å	169.6	94.6
b, Å	49.0	94.6
c, Å	107.0	320.8
	$\beta = 122.4$	$\gamma = 120$
Resolution, Å	50–2.4 (2.49–2.40)	50–2.7 (2.80–2.70)
No. of total reflections	86,210	18,9178
No. of unique reflections	28,189	24,161
Completeness, %	94.3 (64.1)	98.8 (89.8)
No. of degrees collected, °	180	90
Redundancy	3.1 (2.2)	7.8 (5.2)
$I/\sigma I$	11 (1.2)	20.5 (2.18)
R_{sym}, %	8.2 (62.3)	8.6 (51.8)
Refinement		
Resolution, Å	45.5–2.7 (2.5–2.4)	44.8–2.7 (2.8–2.7)
R_{work}, %	19.8 (27.4)	*24.7 (32.8)*
R_{free}, %	23.5 (37.6)	28.2 (43.9)
No. of atoms	4,813	4,949
Protein	4,690	4,856
N-acetylglucosamine	14	14
Water	109	79
Residue range built		
KIT D4D5	310–446/449–463/466–508	311–444/448–465/469–509
Fab light chain	3–212	2–216
Fab heavy chain	1–130/142–192/197–217	0–219
Model quality		
rmsd bond length, Å	0.004	0.004
rmsd bond angles, °	0.770	0.756
B-factor, Å		
Average overall	51.9	56.05
KIT D4	41.8	49.85
KIT D5	49.4	64.88
Fab light chain	61.4	63.9
Fab heavy chain	49.4	48.18
N-acetylglucosamine	31.7	32.18
Water	39.6	40.96
Fab elbow angle, °	143	163
MolProbity		
Ramachandran plot, % favored/outliers	95.95/0.34	95.0/0.2
MolProbity score	2.29	2.26
PDB accession code	4K94	4K9E

Values in parentheses indicate the highest-resolution bin.

Table S2. Summary of interface between Fab19 and KIT$_{D4-5}$

Chain 1	$^{i}N_{res}$ KIT$_{D4-5}$	Chain 2	$^{i}N_{res}$ Fab	Interface area, Å^2		N_{HB}
KIT$_{D4-5}$	18	Heavy chain	13	KIT$_{D4-5}$ 762	Heavy chain 800	9
KIT$_{D4-5}$	3	Light chain	5	KIT$_{D4-5}$ 267	Light chain 283	2

Summary of interface between Fab19 and KIT$_{D4-5}$, calculated using PDBsum web service (13). $^{i}N_{res}$, number of residues involved in interface formation; N_{HB}, number of residues involved in hydrogen bond formation.